PNAS RESEARCH ARTICLE | NEUROSCIENCE OPEN ACCESS

Learning-dependent gating of hippocampal inputs by frontal interneurons

Chun-Lei Zhang[a,1,2], Lucile Sontag[a], Ruy Gómez-Ocádiz[a,3,4], and Christoph Schmidt-Hieber[a,b,2]

Affiliations are included on p. 9.

Edited by John O'Keefe, University College London, United Kingdom; received February 16, 2024; accepted September 3, 2024

The hippocampus is a brain region that is essential for the initial encoding of episodic memories. However, the consolidation of these memories is thought to occur in the neocortex, under guidance of the hippocampus, over the course of days and weeks. Communication between the hippocampus and the neocortex during hippocampal sharp wave-ripple oscillations is believed to be critical for this memory consolidation process. Yet, the synaptic and circuit basis of this communication between brain areas is largely unclear. To address this problem, we perform in vivo whole-cell patch-clamp recordings in the frontal neocortex and local field potential recordings in CA1 of head-fixed mice exposed to a virtual-reality environment. In mice trained in a goal-directed spatial task, we observe a depolarization in frontal principal neurons during hippocampal ripple oscillations. Both this ripple-associated depolarization and goal-directed task performance can be disrupted by chemogenetic inactivation of somatostatin-positive (SOM^+) interneurons. In untrained mice, a ripple-associated depolarization is not observed, but it emerges when frontal parvalbumin-positive (PV^+) interneurons are inactivated. These results support a model where SOM^+ interneurons inhibit PV^+ interneurons during hippocampal activity, thereby acting as a disinhibitory gate for hippocampal inputs to neocortical principal neurons during learning.

hippocampus | prefrontal cortex | sharp wave-ripples | memory consolidation

Significance

Communication between two brain regions, the hippocampus and the neocortex, is thought to be critical for long-term memory storage. Here, we investigate how this process takes place at the level of synaptic inputs to the neocortex. Using electrophysiological in vivo recordings from the hippocampus and the neocortex of mice at different stages of learning a task, we find that a certain class of neurons in the neocortex, so-called somatostatin-positive (SOM^+) interneurons, acts as "gatekeeper" during information transfer from the hippocampus to the neocortex during memory consolidation. Our results suggest that these interneurons are critical for long-term memory storage, and in line with this idea, we show that artificial inactivation of these neurons disrupts task performance.

While the hippocampus is a critical brain structure for episodic memory formation, it is only a part of a complex system distributed across the brain that orchestrates storage, consolidation, and recall of these memories. Once memory representations have formed in the hippocampus, they are broadcast in a time-compressed manner to a wide area of the neocortex (1–5), where they are processed to drive behavior (6–9). This communication is believed to take place during hippocampal sharp-wave ripples (SWRs), which are high-frequency extracellular oscillations (150 to 250 Hz) that occur during slow-wave sleep, quiet wakefulness, or consummatory behaviors (10–13). The replay of hippocampal neuronal sequences during ripples, recapitulating recent experience, has been suggested to be essential for establishing and strengthening neocortical ensembles that represent consolidated memories: If hippocampal ripples are inhibited, memory consolidation is disrupted, and if, conversely, the neocortex is stimulated during SWRs, memory consolidation is enhanced (6, 14–19). Hippocampal ripples are therefore thought to represent an electrophysiological signature of memory consolidation processes marking distinct temporal windows for communication between the hippocampus and neocortical regions, with the prefrontal cortex playing a leading role in the representation of consolidated episodic memories (6, 14–16, 18, 20).

Ripples are most prominent in the CA1 subregion of the hippocampal formation (11), which provides direct excitatory inputs to principal neurons in various frontal subregions (21–24), but also recruits feed-forward inhibition mediated by GABAergic interneurons (25–30). Hippocampal inputs contact both parvalbumin (PV^+) and somatostatin (SOM^+) interneurons (22, 31). PV^+ interneurons mainly exert fast and strong perisomatic inhibition on principal neurons and other PV^+ interneurons, whereas SOM^+ interneurons mainly form inhibitory synapses on distal dendrites of principal neurons and PV^+ interneurons (32–36).

While theories of memory consolidation point to an essential role for hippocampal inputs in establishing neocortical ensembles, how these synaptic inputs are integrated, processed, and weighted in neocortical circuits is still unknown. To address this question, we perform simultaneous in vivo local field potential (LFP) recordings in the hippocampus and whole-cell patch-clamp recordings in the frontal cortex of head-fixed mice performing a goal-directed task. We observe that most frontal neurons show membrane potential depolarizations during hippocampal ripples after animals have learned a goal-directed spatial task. To assess the role of different interneuron

The authors declare no competing interest.

This article is a PNAS Direct Submission.

[1]Present address: Sorbonne Université, Institut de Biologie Paris Seine, Neurosciences Paris Seine, Team Synaptic Plasticity and Neural Networks, F-75005 Paris, France.

[2]To whom correspondence may be addressed. Email: jachin.new1630@gmail.com or christoph.schmidt-hieber@uni-jena.de.

[3]Present address: Department of Neuroscience, Karolinska Institutet, 17177 Stockholm, Sweden.

[4]Present address: Center for Neurology, Academic Specialist Center, Stockholm Health Services, 11365 Stockholm, Sweden.

This article contains supporting information online at https://www.pnas.org/lookup/suppl/doi:10.1073/pnas.2403325121/-/DCSupplemental.

Published October 28, 2024.

subpopulations involved in this ripple-associated depolarization, we chemogenetically suppress the activity of local PV^+ or SOM^+ cells while recording from principal neurons in the medial secondary motor cortex (MOs), revealing distinct roles for different interneuron subtypes in shaping SWR-associated membrane potential dynamics and learning during memory processing.

Results

To study the effects of a spatial learning task on neuronal dynamics, we used an immersive virtual reality (VR) setup adapted for rodent head-fixed navigation (37, 38) (Fig. 1 *A* and *B*). We trained mice to stop in a reward zone near the end of a linear VR corridor (Fig. 1 *A* and *B*). Mice learned to stop for rewards within ~6 d of training (Fig. 1 *A* and *C–E* and *SI Appendix*, Fig. S1 *A–C*). To disentangle spatial learning from a simple association of sensory stimuli with reward delivery, two further groups of mice were subject to different behavioral paradigms: One group was habituated to the VR environment without delivery of any rewards, while another group was passively exposed to the environment by presenting previously recorded VR videos and delivering rewards at randomized positions (Fig. 1*B* and *SI Appendix*, Fig. S1 *D–G*). During passive exposure, animals typically ran with a similar pattern of running and resting periods as during active exploration (*SI Appendix*, Fig. S1 *E–G*).

The medial secondary motor cortex (MOs or M2) is considered a subdivision of the rodent prefrontal cortex (40, 41) that serves as an essential hub for integrating multisensory and spatial information and organizing motor output during voluntary action (37, 41–46). To explore how frontal cortical neurons are synaptically engaged during hippocampal ripples, we obtained in vivo whole-cell patch-clamp recordings from anterior medial MOs neurons while simultaneously performing LFP recordings in the dorsal hippocampal CA1 region (Fig. 2 *A–D* and *SI Appendix*, Fig. S2). The majority of hippocampal ripples occurred when the mouse was resting (mean speed <1 cm/s during ripple periods in >90% of all recorded ripples; *SI Appendix*, Fig. S2*A*), but no reward delivery occurred during any of the ripple periods (*SI Appendix*, Fig. S2*B*). After mice had learned the task, most recorded frontal neurons showed a transient membrane potential depolarization during hippocampal ripples (Fig. 2 *E–H* and *SI Appendix*, Fig. S3). Such a ripple-associated depolarization was not observed in the untrained, VR-habituated, or passively exposed groups of mice (Fig. 2 *G–I*). Intrinsic membrane properties of MOs neurons and dynamics of hippocampal ripples were not significantly affected by the VR training experience (*SI Appendix*, Figs. S4–S6): Spontaneous firing rates were not

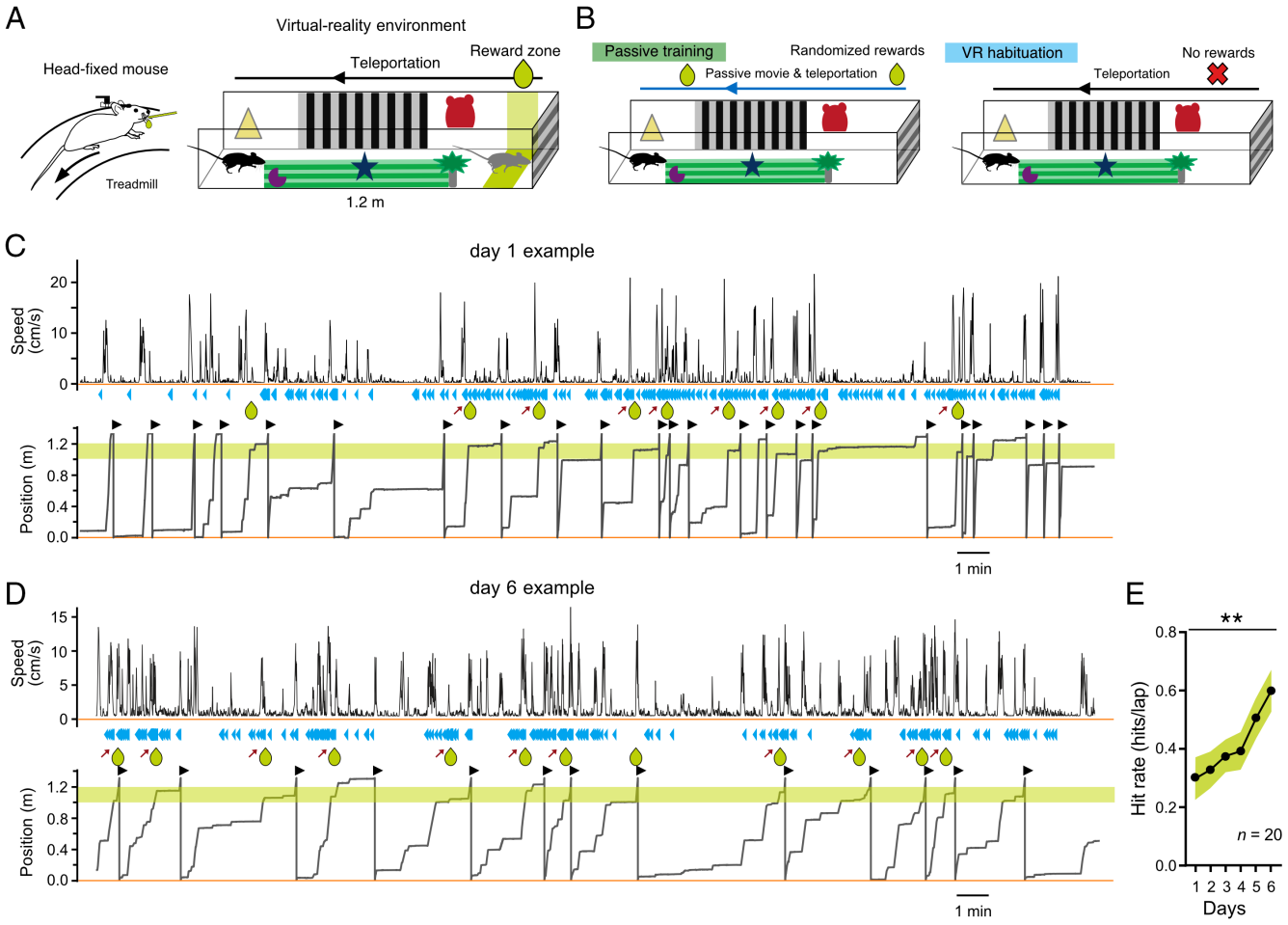

Fig. 1. Mice learn to stop for a reward in a virtual linear corridor. (*A*) *Left*, Schematic drawing of a head-fixed mouse running in a virtual-reality (VR) environment. *Right*, Illustration of a goal-directed learning task implemented in the VR environment. (*B*) Variations of the VR task where mice were either passively exposed to prerecorded VR sessions (*Left*) or only habituated to the VR environment without any reward delivery (*Right*). Partly adapted from scidraw.io (39), which is licensed under CC BY 4.0. (*C* and *D*) Example behavioral data during two training sessions. In each panel, top traces show mouse speed, bottom traces show mouse position on the virtual-reality track, green drops indicate dispensed rewards, blue triangles indicate licks, black triangles indicate teleportation, and red arrows indicate successful licks during reward periods. The green shaded region represents the reward zone. (*E*) Task performance across six days ($n = 20$ mice; hit rate: day 1, 0.30 ± 0.07 hits/lap, versus day 6, 0.60 ± 0.07 hits/lap; repeated measures (RM) one-way ANOVA, $^{**}P = 0.0026$, $F = 3.98$, df = 5). Black trace and shaded regions represent mean ± SEM.

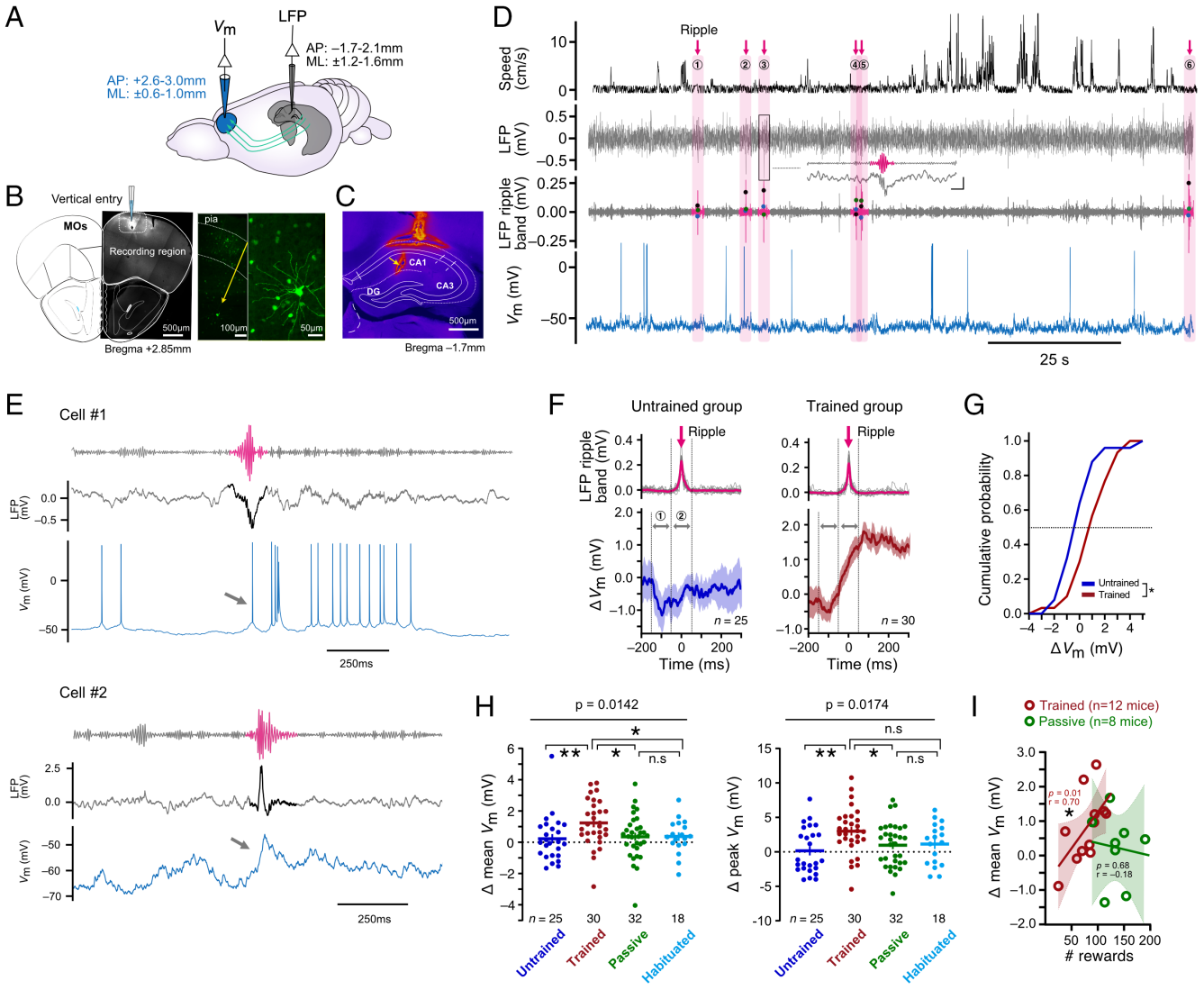

Fig. 2. Membrane potential depolarization emerges in frontal neurons during hippocampal ripples after a spatial learning experience. (*A*) Schematic drawing of recording locations. Whole-cell patch-clamp recordings were performed in the frontal secondary motor cortex (MOs) region (blue), and extracellular local field recording (LFP) recordings were performed in the dorsal hippocampus (gray). Partly adapted from scidraw.io (47), which is licensed under CC BY 4.0. (*B*) *Left*, coronal section of the frontal cortex indicating the recording region in MOs (labeled by fluorescent marker BODIPY); *Right*, biocytin-filled principal neuron in the deep layers of MOs. (*C*) Coronal section of the dorsal hippocampus. The LFP electrode track ending in CA1 is indicated with a yellow arrow. (*D*) Example whole-cell recording from a MOs neuron and simultaneous LFP recording from dorsal CA1 of a mouse running in the VR environment. Traces show (from *Top*) mouse speed (black), raw hippocampal LFP, hippocampal LFP band-pass filtered at 100 to 200 Hz (gray), and membrane potential recording from a MOs principal neuron (blue). Six ripple periods are highlighted (pink). The third ripple period is shown at higher magnification as an inset. (Scale bars, 50 ms, 0.5 mV.) (*E*) Example membrane potential dynamics in MOs neurons during hippocampal ripples (pink). Traces show (from *Top*) band-pass filtered hippocampal LFP (100 to 200 Hz), raw hippocampal LFP, and membrane potential. Hippocampal ripples are highlighted in pink. Note action potential firing during hippocampal ripples in cell #1 and ripple-associated depolarization in cell #2 (arrows). (*F*) Mean membrane potential dynamics in MOs neurons during hippocampal ripples. Data were aligned to the maximal amplitude of the ripple band envelope (*Top* traces) at $t = 0$ s. Colored thick traces represent mean, shaded regions represent ± SEM across recordings from untrained mice (blue, $n = 25$ recordings from 10 mice) or actively trained mice (red, $n = 30$ recordings from 12 mice). "1" and "2" denote baseline and ripple periods, respectively (ripple period: ± 50 ms surrounding the maximal amplitude of the ripple band envelope; baseline period: 100 ms preceding the ripple period). (*G*) Cumulative distribution of ripple-associated Δ mean *Vm* in the untrained (blue) and the trained (red) groups. Kolmogorov–Smirnov test, $^*P = 0.0255$. (*H*) Summary of the data. Membrane potential change during ripples (Δ*Vm*) was computed as the difference between the mean membrane potential (*Left panel*) or the peak membrane potential (*Right panel*) during the ripple period (*Materials and Methods*). *Left panel*: Δ mean *Vm* in trained mice (1.23 ± 0.28 mV) compared with untrained (0.22 ± 0.30 mV, Mann–Whitney *U* test, $^{**}P = 0.0038$), VR habituated (0.37 ± 0.27 mV, $n = 18$ recordings from 9 mice, Mann–Whitney *U* test, $^*P = 0.0265$) or passively trained mice (0.35 ± 0.26 mV, $n = 32$ recordings from 8 mice, Mann–Whitney *U* test, $^*P = 0.0162$). Passively trained versus VR habituated mice, Mann–Whitney *U* test, $P = 0.9601$, ns, not statistically significant. Kruskal–Wallis test, $^*P = 0.0142$. *Right* panel: Δ peak *Vm* in trained mice (2.99 ± 0.63 mV) compared with untrained (0.15 ± 0.68 mV, Mann–Whitney *U* test, $^{**}P = 0.0038$), VR habituated (1.13 ± 0.72 mV, Mann–Whitney *U* test, $P = 0.0717$) or passively trained mice (0.96 ± 0.57 mV, Mann–Whitney *U* test, $^*P = 0.0197$). Passively trained versus VR habituated mice, Mann–Whitney *U* test, $P = 0.8807$, ns, not statistically significant. Kruskal–Wallis test, $^*P = 0.0174$. Filled circles represent individual recordings, error bars represent ± SEM. (*I*) In the trained group, ripple-associated Δ mean *Vm* correlates with the number of rewards that a mouse has received throughout its training, but not in the passively exposed group. Each circle represents the mean ripple-associated Δ mean *Vm* from recordings of the same mouse. Spearman correlation for passively trained mice, $P = 0.6756$, $r = -0.1796$, and trained mice, $^*P = 0.0142$, $r = 0.6993$.

significantly different between trained and untrained animals (*SI Appendix*, Fig. S5*A*) and there was no significant correlation between the ripple-associated membrane potential change and spontaneous firing rates (*SI Appendix*, Fig. S5 *C-E*). Furthermore, intrinsic excitability, as determined by the f–I curve, was not significantly different between trained and untrained animals (*SI Appendix*, Fig. S4*E*), indicating that the observed changes in ripple-associated membrane potential dynamics are unlikely to arise from general increases in network excitability after training. Notably, the number of rewards acquired by a mouse throughout all its training sessions

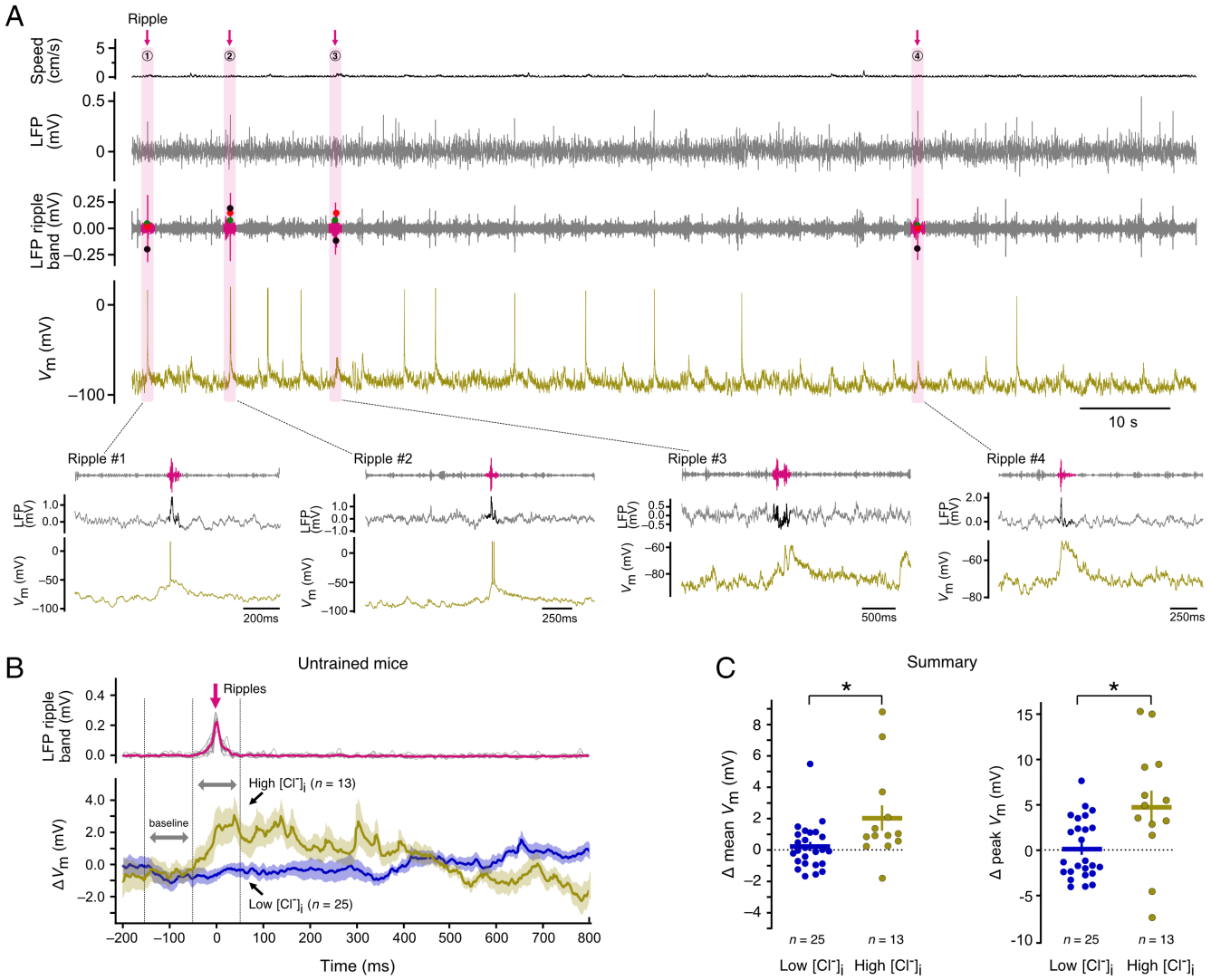

Fig. 3. Elevated intracellular chloride concentration unmasks a ripple-associated depolarization in MOs neurons of untrained mice. (*A*) Example whole-cell recording from a MOs neuron using high $[Cl^-]$, and simultaneous LFP recording from dorsal CA1 of an untrained resting mouse. Traces show (from *Top*): mouse speed (black), raw hippocampal LFP, band-pass filtered hippocampal LFP (100 to 200 Hz, gray), membrane potential (mustard). Four ripple periods are highlighted (pink) and shown below at higher magnification. (*B*) Mean membrane potential dynamics in MOs neurons during hippocampal ripples. Data are presented as in Fig. 2*F* (n = 13 recordings from 6 mice using high Cl^- internal solution, and n = 25 recordings using low Cl^- internal solution). *Top* traces (ripple envelope) were obtained in the high $[Cl^-]_i$ group. Data in low $[Cl^-]_i$ are the same as shown in Fig. 2*F* (untrained group). Note ripple-associated depolarization in MOs neurons during recordings in high $[Cl^-]_i$. (*C*) Summary of the data. Membrane potential change during ripples (ΔVm) was computed as the difference between the mean membrane potential (*Left panel*) or the peak membrane potential (*Right panel*) during the ripple period (*Materials and Methods*). *Left* panel: Δ mean *Vm* when using high $[Cl^-]_i$ (mustard, 2.02 ± 0.85 mV) compared to recordings in low $[Cl^-]_i$ (0.22 ± 0.30 mV) in untrained mice. Mann–Whitney *U* test, $^*P = 0.0179$. *Right* panel: Δ peak *Vm* when using high $[Cl^-]_i$ (5.02 ± 1.88 mV) compared to recordings in low $[Cl^-]_i$ (0.15 ± 0.68 mV) in untrained mice. Mann–Whitney *U* test, $^*P = 0.0103$. Data are analyzed and presented as in Fig. 2*H*. Data in low $[Cl^-]_i$ are the same as in Fig. 2*H* (untrained group).

correlated with the ripple-associated depolarization amplitude in the trained group, but not in the passively exposed group (Fig. 2*I* and *SI Appendix*, Fig. S1 *H* and *I*). The average running speeds of the animals did not correlate with the ripple-associated depolarization amplitude in both groups (*SI Appendix*, Fig. S1*J*). Together, our results suggest that the frontal neuronal depolarization during hippocampal ripples is associated with learning of the task.

Experience-dependent plasticity of inhibitory circuits plays a critical role in neuronal network adaptations during memory processing (48–50). To probe the role of inhibition in the observed learning-dependent ripple-associated depolarization, we increased the Cl^- concentration in the recording pipette solution ($[Cl^-]_i$), thereby shifting the $GABA_A$ receptor reversal potential (E_{GABA}) close to 0 mV (Fig. 3*A*), without changing intrinsic membrane properties of MOs neurons in vivo (*SI Appendix*, Fig. S7 *A–F*). Under these high $[Cl^-]_i$ recording conditions, a ripple-associated depolarization was revealed in untrained mice (Fig. 3 *B* and *C*) where it had previously not been observed with normal $[Cl^-]_i$ (Fig. 2 *F* and *H*). These results indicate that activated GABAergic inhibitory inputs balance excitatory inputs during ripples before the learning experience, raising the possibility that disinhibition underlies the learning-induced ripple-associated depolarization in trained mice (*SI Appendix*, Fig. S7 *G* and *H*).

To further explore this possibility, we next sought to test the role of interneuron subpopulations in shaping the ripple-associated depolarization. To consistently suppress the activity of local parvalbumin-positive (PV^+) or somatostatin-positive (SOM^+) interneurons in MOs throughout ripple periods, we chemogenetically inactivated either PV^+ or SOM^+ interneurons while recording the membrane potential of principal neurons (Fig. 4*A*). A chemogenetic strategy was chosen because the ripple-associated depolarization started with the onset of any detectable change in the ripple envelope (Fig. 2 *E* and *F*), so that a closed-loop optogenetic strategy triggered by a

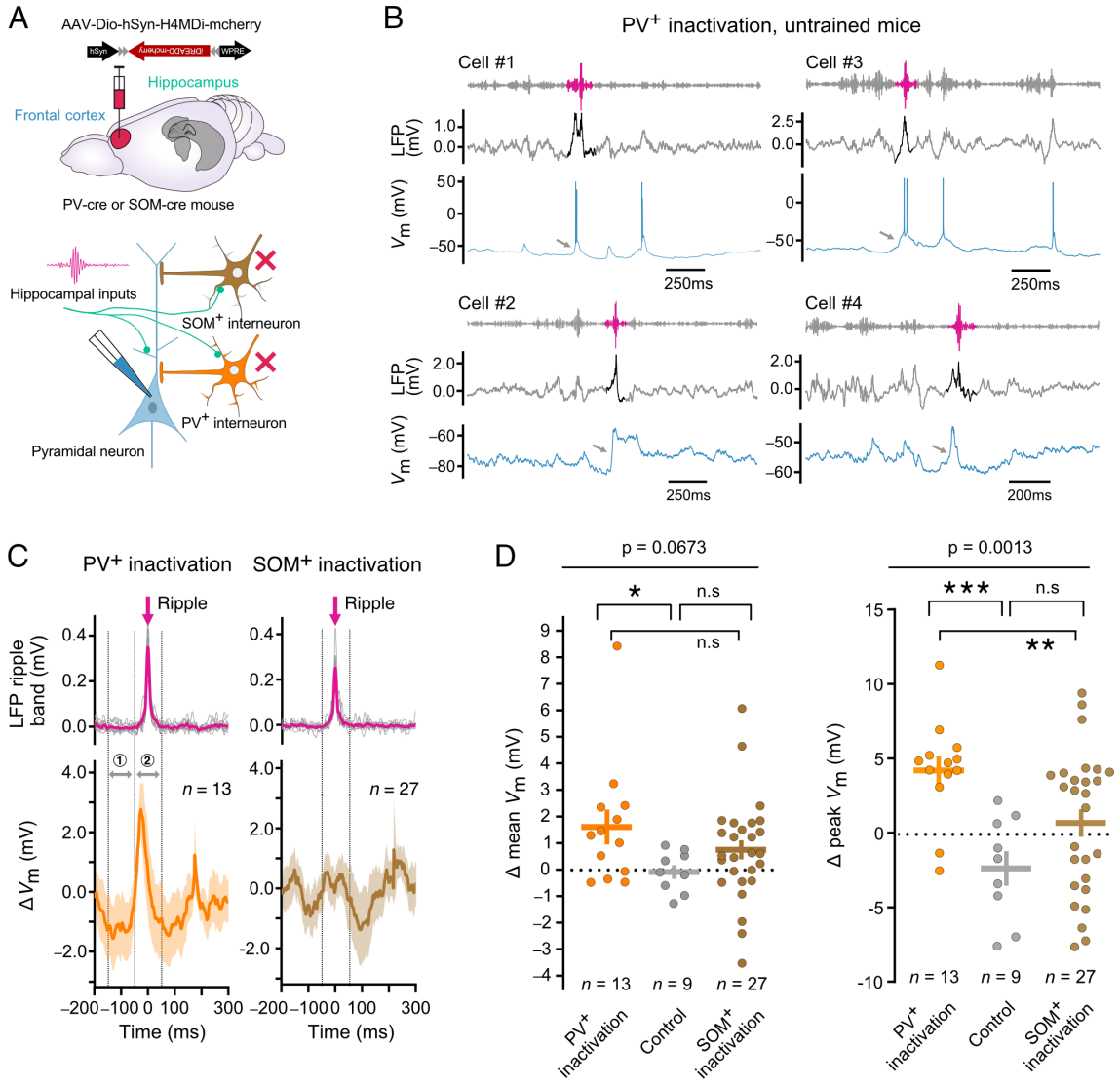

Fig. 4. Inactivation of PV$^+$ interneurons unmasks a ripple-associated depolarization in MOs neurons of untrained mice. (*A*) Schematic drawing of the experimental paradigm. PV$^+$ (orange) or SOM$^+$ interneurons (brown) were chemogenetically inactivated in frontal circuits using Cre-dependent expression of the inhibitory DREADD h4MDi. Partly adapted from scidraw.io (51, 52), which is licensed under CC BY 4.0. (*B*) Example membrane potential dynamics in MOs neurons during hippocampal ripples in untrained mice during inactivation of frontal PV$^+$ interneurons. Traces show (from *Top*) band-pass filtered hippocampal LFP (100 to 200 Hz), raw hippocampal LFP, and membrane potential. Hippocampal ripples are highlighted in pink. Note ripple-associated depolarizations (arrows). (*C*) Mean membrane potential dynamics in MOs neurons during hippocampal ripples. Data are presented as in Fig. 2*F* (n = 13 recordings from 7 mice during inactivation of PV$^+$ interneurons, and n = 27 recordings from 8 mice during inactivation of SOM$^+$ interneurons). (*D*) Summary of the data. Membrane potential change during ripples (Δ*V*m) was computed as the difference between the mean membrane potential (*Left panel*) or the peak membrane potential (*Right panel*) during the ripple period (*Materials and Methods*). *Left panel*: Δ mean *V*m during inactivation of PV$^+$ interneurons (1.60 ± 0.68 mV), compared with control conditions (n = 9 recordings from 3 mice, −0.09 ± 0.27 mV, Mann–Whitney *U* test, **P* = 0.0208; CNO, i.p in PV-Cre mice transfected with AAV-CAG-FLEX-tdTomato in frontal regions) and inactivation of SOM$^+$ interneurons (0.70 ± 0.38 mV, Mann–Whitney *U* test, *P* = 0.3028, ns). CNO control versus SOM$^+$ interneurons, Mann–Whitney *U* test, *P* = 0.1008, ns. Kruskal–Wallis test, *P* = 0.0673. *Right panel*: Δ peak *V*m during inactivation of PV$^+$ interneurons (4.19 ± 0.98 mV), compared with control conditions (−2.39 ± 1.23 mV, Mann–Whitney *U* test, ****P* = 0.0004) and inactivation of SOM$^+$ interneurons (0.66 ± 0.94 mV, Mann–Whitney *U* test, ***P* = 0.0061). CNO control versus SOM$^+$ interneurons, Mann–Whitney *U* test, *P* = 0.0794, ns. Kruskal–Wallis test, ***P* = 0.0013. Data are analyzed and presented as in Fig. 2*H*.

ripple detection algorithm would likely have failed to inactivate interneurons before the depolarization had started. Importantly, chemogenetic inactivation of PV$^+$, but not of SOM$^+$ interneurons, unmasked a depolarization during ripples in most MOs principal neurons of untrained mice (Fig. 4 *B*–*D*). The peak amplitude of this depolarization was larger during inactivation of PV$^+$ interneurons than during inactivation of SOM$^+$ interneurons (Fig. 4*D*). This unmasking effect during PV$^+$ inactivation was specific to the ripple band as it could not be detected when membrane potential was aligned to higher-frequency LFP events outside of the ripple band (*SI Appendix*, Fig. S8 *I* and *J*). In line with our previous report (37), chemogenetic inactivation of PV$^+$ interneurons affected the activity of frontal neurons without changing their intrinsic membrane properties (*SI Appendix*, Fig. S8 *A*-*G*). These results suggest that the depolarization that emerges after training can be explained by disinhibition of most principal neurons caused by reduced activity of PV$^+$ interneurons during hippocampal ripples in a feed-forward circuit (37) (Fig. 4*D* and *SI Appendix*, Fig. S8*H*).

Accumulating evidence suggests that excitatory inputs to SOM$^+$ interneurons undergo task-specific experience-dependent plasticity (53, 54), resulting in disinhibition of principal neurons by SOM$^+$ mediated inhibition of PV$^+$ interneurons after learning (37). To test whether this process plays a role during learning in MOs, we next examined whether inactivation of PV$^+$ or SOM$^+$ interneurons affects goal-directed behavior and learning-dependent ripple-associated depolarizations (Fig. 5). After training, we found that inactivation of

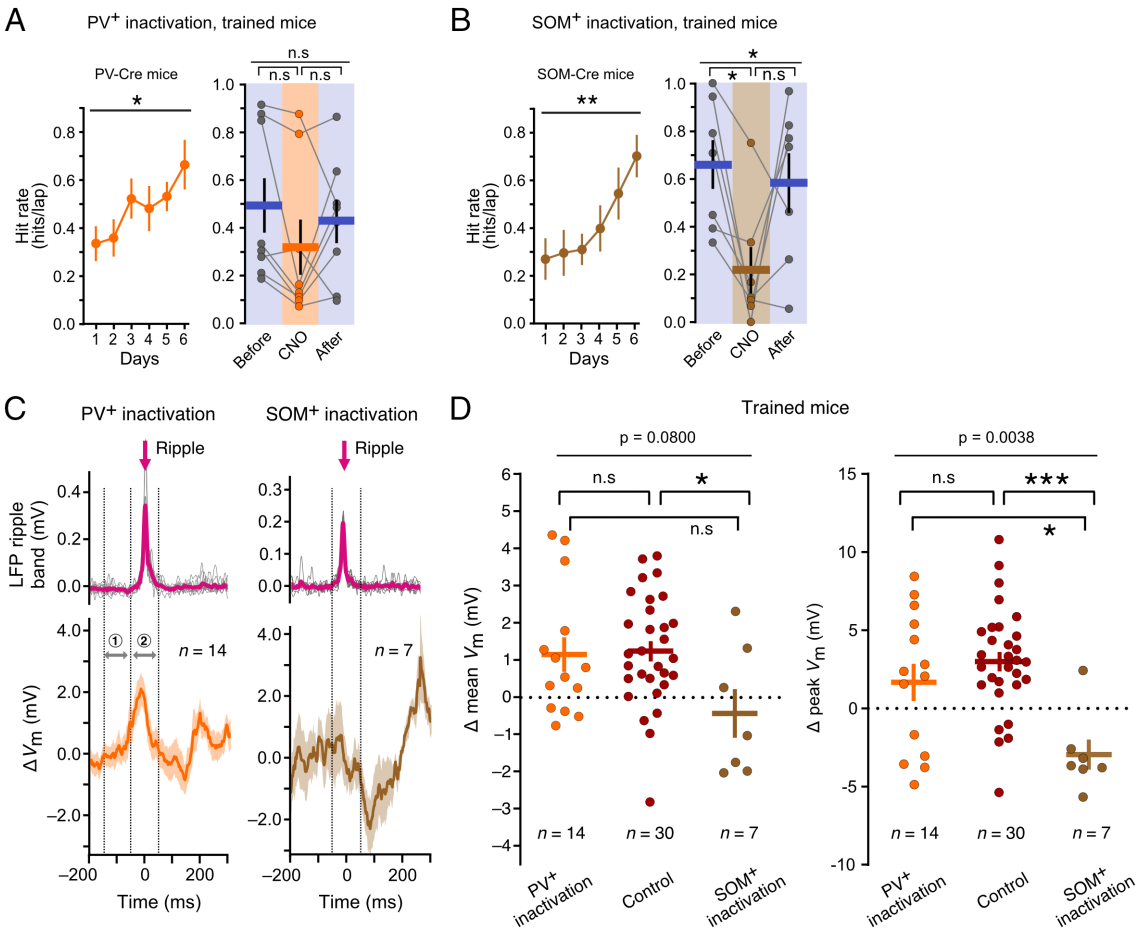

Fig. 5. Inactivation of SOM$^+$ interneurons in MOs disrupts ripple-associated depolarization and goal-directed behavior. (*A*) Training performance of mice expressing h4MDi in PV$^+$ MOs interneurons quantified as hit rate (hits/lap). *Left*, training performance across days (day 1, 0.34 ± 0.08 hits/lap, versus day 6, 0.66 ± 0.11 hits/lap, n = 10 mice; RM one-way ANOVA, *P = 0.0315, F = 2.72, df = 5). *Right*, behavioral performance was assessed after completion of training. Hit rate on the day before (0.49 ± 0.12 hits/lap, n = 8 mice), during (CNO application, 0.32 ± 0.12 hits/lap), and after bilateral inactivation of PV$^+$ interneurons in MOs (0.43 ± 0.10 hits/lap). RM one-way ANOVA, P = 0.1646, F = 2.15, df = 2; post hoc Dunnett's test, day before versus CNO application, P = 0.1034; CNO application versus day after, P = 0.5028. Error bars represent ± SEM. (*B*) Training performance of mice expressing h4MDi in SOM$^+$ MOs interneurons quantified as hit rate (hits/lap). *Left*, training performance across days (day 1, 0.27 ± 0.09 hits/lap, versus day 6, 0.70 ± 0.09 hits/lap, n = 10 mice; RM one-way ANOVA, **P = 0.0014, F = 4.79, df = 5). *Right*, behavioral performance was assessed after completion of training. Hit rate on the day before (0.66 ± 0.11 hits/lap, n = 7 mice), during (CNO application, 0.22 ± 0.11 hits/lap), and after bilateral inactivation of SOM$^+$ interneurons in MOs (0.58 ± 0.14 hits/lap). RM one-way ANOVA, *P = 0.0308, F = 5.19, df = 2; post hoc Dunnett's test, day before versus CNO application, *P = 0.0160; CNO application versus day after, P = 0.1237. (*C*) Mean membrane potential dynamics in MOs neurons of trained mice during hippocampal ripples. Data are presented as in Fig. 2*F* (n = 14 recordings from 4 mice during inactivation of PV$^+$ interneurons, and n = 7 recordings from 3 mice during inactivation of SOM$^+$ interneurons). (*D*) Summary of the data. Membrane potential change during ripples (Δ*V*m) was computed as the difference between the mean membrane potential (*Left panel*) or the peak membrane potential (*Right panel*) during the ripple period (*Materials and Methods*). *Left panel*: Δ mean *V*m during PV$^+$ inactivation (1.14 ± 0.48 mV), in control conditions (1.23 ± 0.28 mV), during SOM$^+$ inactivation (−0.44 ± 0.71 mV). PV$^+$ inactivation versus control, Mann–Whitney *U* test, P = 0.5250; SOM$^+$ inactivation versus control, Mann–Whitney *U* test, *P = 0.0291; PV$^+$ inactivation versus SOM$^+$ inactivation, Mann–Whitney *U* test, P = 0.0938. Kruskal–Wallis test, P = 0.0800. *Right panel*: Δ peak *V*m during PV$^+$ inactivation (1.67 ± 1.24 mV), in control conditions (2.99 ± 0.63 mV), during SOM$^+$ inactivation (−2.95 ± 1.04 mV). PV$^+$ inactivation versus control, Mann–Whitney *U* test, P = 0.4468; SOM$^+$ inactivation versus control, Mann–Whitney *U* test, ***P = 0.0002; PV$^+$ inactivation versus SOM$^+$ inactivation, Mann–Whitney *U* test, *P = 0.0250. Kruskal–Wallis test, **P = 0.0038. Data are analyzed and presented as in Fig. 2*H*. Data in control conditions are the same as shown in Fig. 2*H* (trained group).

SOM$^+$, but not of PV$^+$ interneurons, disrupted goal-directed behavioral performance (Fig. 5 *A* and *B*). The observation that SOM$^+$ interneuron activity is still required to perform the task after training suggests that the neocortical assemblies are not yet fully independent of the hippocampus at this early point of learning, and that hippocampal inputs are still essential to recruit these assemblies (55). We further analyzed motor behavior by comparing the durations and frequencies of running and resting periods. Inactivation of SOM$^+$ interneurons led to an increased frequency of running periods without affecting their durations (*SI Appendix*, Fig. S9). Importantly, the frequency and duration of resting periods was not significantly affected by SOM$^+$ inactivation (*SI Appendix*, Fig. S9 *K* and *L*), making it unlikely that the observed changes in task performance are caused indirectly by alterations in motor patterns which may affect ripple occurrence, consistent with the finding that overall ripple occurrence rates were not significantly different across animal groups (*SI Appendix*, Fig. S6*H*). Furthermore, inactivation of SOM$^+$, but not of PV$^+$ interneurons, abolished the learning-dependent ripple-associated depolarization (Fig. 5 *C* and *D*), suggesting a specific role for frontal SOM$^+$ interneurons in shaping the circuit response to behavioral training in the goal-directed task.

Discussion

Recent work has revealed an essential role for inhibitory circuits in learning and memory across various brain regions (50, 56, 57). To determine how excitatory and inhibitory inputs are integrated in frontal neurons during systems consolidation, here we have performed in vivo membrane potential recordings from MOs neurons while simultaneously recording the local field potential

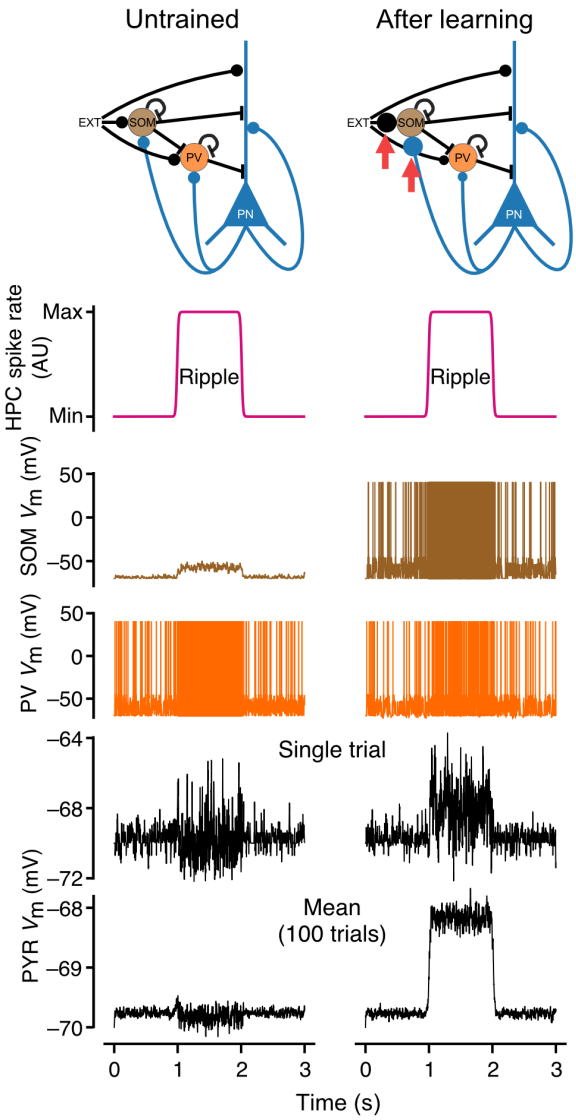

Fig. 6. SOM$^+$ plasticity reproduces learning-dependent depolarization in a computational model of the MOs microcircuit. The model consists of a SOM$^+$ interneuron, a PV$^+$ interneuron, and a principal neuron (schematic at *Top*). Traces show (from *Top*) spike rates of ripple-associated external inputs to MOs, membrane potential of the SOM$^+$ interneuron, membrane potential of the PV$^+$ interneuron, membrane potential of the principal neuron in a single simulation trial, and mean membrane potential of the principal neuron across 100 simulation trials. The effect of learning was implemented by increasing the synaptic weights of excitatory synapses to SOM$^+$ interneurons, thereby reproducing the experimentally observed depolarization during ripples in the principal neurons (*Right* column).

in CA1 of mice at different stages of learning of a goal-directed task. We show that local PV$^+$ and SOM$^+$ inhibitory interneurons play distinct roles in shaping learning-dependent neocortical circuit dynamics during hippocampal ripples: PV$^+$ interneurons control the depolarization of principal neurons during ripples, while activation of SOM$^+$ interneurons following a learning experience leads to inhibition of PV$^+$ interneurons and consequently to disinhibition of principal neurons during ripples.

SOM-expressing interneurons are composed of several subtypes, with some predominantly inhibiting the apical dendrites of principal neurons (35, 58–60) while others mainly inhibit PV$^+$ interneurons, thereby disinhibiting principal neurons (22, 34, 61). Our finding that the ripple-associated depolarization and goal-directed performance can be disrupted by inactivation of SOM$^+$ interneurons suggests that the latter type of disinhibitory SOM$^+$ interneurons is predominantly involved in learning-dependent reconfiguration of neocortical circuits (37, 53, 54). We propose that increased activation of SOM$^+$ interneurons during learning preferentially inhibits PV$^+$ interneurons during hippocampal ripples, thereby increasing the relative weight of direct excitatory hippocampal inputs or indirect inputs generated by feedback loops from other neocortical areas (62, 63).

This scenario is consistent with a computational model of the MOs microcircuit that we have developed, where increased weights of excitatory synapses on SOM$^+$ interneurons during learning lead to inhibition of PV$^+$ interneurons and consequently to disinhibition of principal neurons (Fig. 6 and *SI Appendix*, Fig. S10). SOM$^+$ interneuron activation will thereby act as a "gate" for information arriving in the neocortex from the hippocampus (55, 57, 64). By opening a window for synaptic plasticity (65, 66), this disinhibition will allow these increased hippocampal excitatory inputs to create or strengthen neocortical assemblies that will represent consolidated memories. Thereby, disinhibition and synaptic plasticity work in conjunction to mediate learning-dependent changes in circuit configurations.

Which behaviors can trigger this gating mechanism? Engagement in a spatial task (67) where rewards are predicted (68) can activate hippocampal synaptic inputs to the neocortex during learning. Here, we find that an active experience where mice learn to acquire rewards at specific locations of the environment lastingly reconfigures neocortical circuits to enhance the weights of hippocampal inputs by disinhibition. Such a reconfiguration of the neocortical network driven by hippocampal ripple oscillations may allow for the potentiation of relevant hippocampal inputs in specific circuits engaged during learning of a goal-directed task, thereby contributing to long-term consolidation of memories supporting a distinct behavior. Together with the finding that goal-directed performance can be disrupted by inactivation of SOM$^+$ interneurons, we have identified a circuit motif that may be causally involved in learning and memory.

Materials and Methods

Animals. All procedures were carried out in accordance with European and French national guidelines on the protection of animals used for scientific purposes (EU Directive 2010/63/EU), and were approved by the Ethics Committee CETEA of the Institut Pasteur (APAFIS#7771-2016112516084126v1). 6- to 12-wk-old wild-type (WT) C57BL/6 J and transgenic mice were kept on a regular 12/12 h light-dark cycle with ad libitum access to food and water. The following Cre mouse lines were obtained from the Jackson Laboratories: SST-Cre (SOM-Cre, no: 013044) and PV-Cre (no: 008069). These mice were backcrossed onto a C57BL/6 J background.

Surgical Procedures and Transduction by Viral Vectors. Surgeries were performed under continuous anesthesia with isoflurane (5% for induction, 1 to 3% for maintenance, vol/vol). Preceding the surgery, mice were treated with intraperitoneal injection of buprenorphine (0.05 mg/kg) and meloxicam (5 mg/kg), and local application of lidocaine (0.4 ml/kg of a 1% solution). Mice were positioned in a stereotaxic apparatus (David Kopf Instruments, Tujunga, CA). A half-circle stainless steel headpost (Luigs & Neumann) was fixed to the mouse skull using dental cement (Super-Bond, Sun Medical Co. Lt). Mice were allowed to recover for 2 wk after headpost implantation. Body temperature was maintained at 37 °C by placing the mice on a heating pad during and after the surgery. Mice were treated postoperatively with meloxicam (5 mg/kg), administered orally in combination with surgical recovery feeding gel (Clear H_2O, BioService).

Circular craniotomies (0.5 to 0.6 mm diameter) were performed above the anterior medial MOs and dorsal hippocampus under isoflurane anesthesia 1 h before the onset of recordings using a dental drill (stereotaxic coordinates from Bregma, anteroposterior [AP] +2.6 to 3.1 mm and mediolateral [ML] ±0.4 to 1.0 mm for MOs; [AP] -1.6 to 2.1 mm and [ML] ±1.0 to 1.6 mm for dorsal

hippocampus). Mice were treated with an intraperitoneal injection of meloxicam (5 mg/kg) at the end of the procedure, and then transferred to the recording setup.

To suppress the activity of PV^+ or SOM^+ interneurons, an adeno-associated viral vector [AAV5-hSyn-DIO-hM4D(Gi)-mCherry, ref Addgene-44362, 7E12 vector genomes (vg)/ml] was injected into the MOs of either PV-Cre or SOM-Cre mice. Another adeno-associated viral vector (AAV1-CAG-FLEX-tdTomato-WPRE, ref Addgene-28306, 1E13 vector genomes (vg)/ml) was used as a control virus. 6- to 8-wk-old male mice were injected with viral vectors (300 to 400 nl per site) into the MOs region (stereotaxic coordinates from Bregma, anteroposterior [AP] + 2.8 to 3.0 mm, mediolateral [ML] ±0.5 to 0.7 mm, 2 injections at 300 μm and 550 μm depth from dura). The virus was bilaterally pressure-injected through glass pipettes (Drummond Wiretrol 10 μl) using an oil-hydraulic micromanipulator (MO-10, Narishige, Japan) at a rate of 100 nl/min. Headpost implantation was performed 3 wk after viral injections.

Virtual-reality Environments. The virtual reality setup was implemented as described previously (37, 38, 69). Head-fixed mice were placed on a cylindrical polystyrene treadmill (20 cm diameter) supported by pressurized air bearings, rotating forward or backward. Cylinder rotation associated with mouse locomotion was read out from the surface of the treadmill with a computer mouse (G700s, Logitech, used in wired mode) at a poll rate of 1 kHz. Briefly, motion on the treadmill was read out as described above and linearly converted to one-dimensional movement along the virtual reality corridor (Fig. 1*C*). The virtual environment was projected onto a spherical dome screen (120 cm diameter), covering nearly the entire field of view of the mouse, using a quarter-sphere mirror (45 cm diameter) and a projector (Casio XJ-A256) located below the mouse. The virtual linear corridor was 1.2 m to 2.2 m long, enriched with objects placed along the linear track and diverse textures on the walls. A reward zone (0.2 m length) was located near the end of the corridor (37, 38). Mice were teleported back to the beginning of the track when they reached the end of the corridor. This virtual reality environment has been shown to produce substantial spatial coding in hippocampal neurons (70). The Blender Game Engine (http://www.blender.org) was used in conjunction with the Blender Python API to drive the virtual reality system.

Behavioral Training and Analysis. Two weeks after the headpost implantation, mice were handled 10 min per day for 3 d. Untrained mice were habituated 15 min per day for 2 to 3 consecutive days on the treadmill in the recording environment. Another group of mice was trained in a goal-directed task in a virtual-reality environment. Controlled water delivery was used to improve motivation during the goal-directed task. At the beginning of experiments, mice were placed under controlled water supply (0.5 g of hydrogel per day, Clear H_2O, BioService) and maintained at ~85% of their initial body weight over the course of behavioral training and electrophysiology experiments. The welfare and weight of mice were checked and documented on a daily basis. After habituation and water deprivation, mice underwent 6 training sessions, 30 to 45 min each, over the course of 1 wk before recordings (Fig. 1 *A* and *C–E*). A drop of sweetened water (10 μl, 8 mg/ml sucrose) was dispensed by a spout as a reward if mice spent 2 s or more within the reward zone. Licks were detected with a piezo element attached to the reward spout. A "hit" was detected when the mouse performed licks within a period of 3 s before the reward delivery. When the mice reached the end of the linear track, they were "teleported" back to the start of the virtual corridor after crossing a black frontal wall, indicating the end of a lap and the onset of the subsequent one. The behavioral performance of the training group was comparable between different sessions (Fig. 1*E* and *SI Appendix*, Fig. S1 *B* and *C*). To disentangle spatial learning from a simple association of sensory stimuli with reward delivery, two further groups of mice were subject to different behavioral paradigms: One group was habituated 30 to 45 min per day for 5 d to the VR environment without delivering any rewards and without water deprivation, while another group was passively exposed to the environment by presenting previously recorded VR videos and delivering rewards at randomized positions (30 to 45 min per day for 6 d; Fig. 1*B*). Performance was quantified as successful predictive licks ("hits") per lap (hits/lap), reward rate (dispensed rewards per lap; rewards/lap), and relative fraction of time in the reward zone (Fig. 1*E* and *SI Appendix*, Fig. S1 *B* and *C*). Motor behavior was further analyzed by comparing the durations and frequencies of running and resting periods (*SI Appendix*, Fig. S9).

In Vivo Chemogenetic Experiments. We observed that the ripple-associated depolarization often started before any substantial rise in the ripple envelope (see e.g. Fig. 2*F*). We therefore decided to use a chemogenetic approach to consistently inactivate interneuron subpopulations throughout ripple events, as any ripple-triggered optogenetic approach would not capture the early phase of the depolarization because of the inherent latency of online ripple detection algorithms.

After viral injection and headpost implantation in MOs as described above, two groups of mice (PV-Cre or SOM-Cre) were habituated to the recording environment during 2 to 3 consecutive days. Clozapine (CNO; Tocris Biosciences; 5 mg/kg) was administered by intraperitoneal injection 30 min prior to electrophysiological recordings (Fig. 4 and *SI Appendix*, Fig. S8) (37). All recordings were performed within 3 h after CNO application. Two more groups of mice expressing h4MDi in PV^+ or SOM^+ MOs interneurons completed a full training schedule over the course of 1 wk before recordings or behavioral tests (Fig. 5). Training performance of mice was quantified to establish their engagement in the task across 6 d (Fig. 5 *A* and *B*). On the 7th day, one group of trained mice was used for electrophysiological recordings (Fig. 5 *C* and *D*). Another group of mice was tested in the task again (denoted as "day before"). On the 8th day, mice were intraperitoneally injected with CNO (5 mg/kg), and behavioral testing was performed 30 to 45 min later (denoted as "CNO application"). On the 9th day, a post-CNO test was performed (denoted as "day after") (Fig. 5 *A* and *B* and *SI Appendix*, Fig. S9).

In Vivo Electrophysiology.

Whole-cell patch-clamp and LFP recordings. Recordings were performed from head-fixed mice placed on the treadmill as previously described (37, 38). Glass pipettes were pulled from borosilicate glass (~5 MΩ pipette resistance) and filled with low [Cl^-] internal solution containing (in mM) 130 potassium methanesulfonate, 7.0 KCl, 0.3 $MgCl_2$, 0.1 EGTA, 10 HEPES, 1 sodium phosphocreatine, 3.0 Na_2ATP, 0.3 NaGTP; or high [Cl^-] internal solution containing (in mM) 137 KCl, 0.3 $MgCl_2$, 0.1 EGTA, 10 HEPES, 1 sodium phosphocreatine, 3.0 Na_2ATP, 0.3 NaGTP. 5 mg/ml biocytin was added to the internal solution to label recorded cells. pH was adjusted to 7.2 with KOH. Osmolarity was 289 mOsm. Whole-cell patch-clamp recordings were obtained using a standard blind-patch approach (69, 71). In brief, a high positive air pressure (~1,000 mbar) was applied to the pipettes before slowly lowering them into the dorsal part of the MOs region via a small craniotomy (~500 μm) using a micromanipulator (Luigs & Neumann Mini In Vivo). Recordings were obtained at a depth of 150 to 420 μm (superficial neurons; typically layers 2/3) or 430 to 900 μm (deep neurons; typically layers 5/6) from the pial surface. At a depth of ~150 μm from the pial surface, the air pressure was decreased to 50 to 80 mbar. Seal resistances were always >1 GΩ, and access resistances were typically 25 to 70 MΩ, with recordings terminated when access resistance exceeded 100 MΩ. Recordings were made in current-clamp mode, and no holding current was applied during recordings. For the analysis, only cells with recording durations exceeding 60 s were included. Typical recordings lasted 5 to 10 min, and longer recordings (~30 min) were occasionally achieved. We restricted our in vivo whole-cell recordings to the current-clamp configuration, as estimates of excitatory and inhibitory synaptic conductances from voltage-clamp recordings in large branching neurons are subject to substantial errors arising from space clamp distortions that are exacerbated by active dendritic conductances (72, 73). As ripples usually occurred during resting states of the mouse (*SI Appendix*, Fig. S2), electrophysiological data for the present study were typically obtained when the mice were resting at the beginning of the track. Part of the whole-cell patch-clamp data used in the present study were used for previous work, where we determined membrane potential dynamics in frontal neurons preceding locomotion (37).

To track hippocampal ripples, a tungsten electrode (~1 MΩ resistance, FHC Info) was connected to an extracellular module (npi electronic EXT-10-2F), and lowered using a micromanipulator (Sensapex uMP-4) into the dorsal hippocampal CA1 region (1.2 to 1.6 mm depth). To record the LFP simultaneously with whole-cell patch-clamp recordings, membrane potential and LFP signals were low-pass filtered at 10 kHz and 1 kHz, respectively (Intan CLAMP system; npi electronic EXT-10-2F with special low-pass filter), and acquired at 50 kHz (Intan Technologies CLAMP system). During recordings, two silver/silver chloride reference electrodes (0.3 mm diameter) were connected to two systems, and positioned in additional small craniotomies close to lambda. Two references are separately positioned and soaked in the bath solution. An external solution containing (in mM) 150 NaCl, 2.5 KCl, 10 HEPES, 2 $CaCl_2$, and 1 $MgCl_2$ (pH 7.2, 289 mOsm) was perfused on top of the craniotomy through a round plastic chamber (4 mm diameter).

Immunohistochemistry and Cell Identification. At the end of recordings, mice were deeply anesthetized with an overdose of ketamine/xylazine (100 mg/kg and 10 mg/kg i.p.) and quickly perfused transcardially with 0.1 M phosphate-buffered saline (PBS) followed by a 4% Formaldehyde solution in PBS (PFA). Brains were removed from the skull and kept in PFA for at least 24 h. 50-μm-thick parasagittal slices were stained with Alexa Fluor 488–streptavidin to reveal biocytin-filled neurons and patch pipette tracts. DAPI was applied as a nuclear stain to reveal the general anatomy of the preparation. Fluorescence images were acquired using a spinning disc confocal microscope (Opterra, Bruker) and analyzed using ImageJ. Neurons were first identified as principal cells according to their characteristic electrophysiological signature (*SI Appendix*, Fig. S4*B*). Whenever the morphological recovery of recorded neurons was successful, this classification was confirmed using the shape and position of biocytin-filled neurons. To confirm the tracts of pipettes or tungsten wires, the fluorophore BODIPY TMR-X (Invitrogen; 5 mM in PBS 0.1 M, DMSO 40%) was painted on the tips in some recordings (Fig. 2*B*).

Data Processing.

In vivo whole-cell electrophysiology data analysis. Input resistance was calculated from the steady-state voltage response to a small hyperpolarizing 500-ms current pulse from baseline membrane potential (*SI Appendix*, Figs. S4, S7, and S8). Baseline membrane potential was measured before current pulse injections at the beginning of the recording. Spontaneous firing rates and membrane potentials were measured across recordings with durations exceeding 60 s. To analyze subthreshold membrane potential, traces were digitally low-pass filtered at 5 kHz and resampled at 10 kHz. Action potentials were then removed by thresholding to determine action potential times and then masking values 2 ms before and 10 to 20 ms after the action potential peak. After spike removal, ripple-associated changes in subthreshold membrane potential (ΔVm) were computed by subtracting the mean of subthreshold membrane potential traces. Ripple-associated ΔVm was computed as the difference in mean *Vm* during the ripple period (50 ms preceding the peak of the ripple band envelope to 50 ms after the peak of the ripple band envelope, unless indicated otherwise) and during the preceding baseline period (150 ms preceding the peak of the ripple band envelope to 50 ms preceding the peak of the ripple band envelope, unless indicated otherwise). As an alternative measure, we also computed the difference between peak *Vm* during the ripple period and mean *Vm* during the preceding baseline period, where the peak was determined as the membrane potential value with the largest absolute difference from the baseline membrane potential (Figs. 2*H*, 3*C*, 4*D.* and 5*D*).

Hippocampal ripple detection. For off-line detection of ripples, LFP data were band-pass filtered in a ripple band (100 to 200 Hz) and in a noise band (300 to 500 Hz). The envelopes of both ripple and noise signals were obtained using the Hilbert transform, yielding A_{ripple} and A_{noise}. When A_{ripple} was below $3xA_{noise}$, we set A_{ripple} to 0 to eliminate periods of high noise caused for example by animal movement. A_{ripple} was then z-scored, yielding a transformed signal $R(t)$. Ripples were defined as events where $R(t)$ crossed the threshold of 10 SD and remained above 1 SD for 20 ms to 300 ms (18). These conservative threshold values were confirmed by visual inspection of the detected ripples, and were chosen to minimize the number of false positive events. Recordings included in the analysis contained at least 3 ripples. To compute ripple-associated ΔVm, traces were aligned to the peak of the ripple envelope of each ripple. To verify that changes in *Vm* were specific to the ripple frequency band, the results obtained for events detected within the ripple band were compared with events detected using a different frequency band (signal: 500 to 800 Hz; noise: 800 to 1500 Hz) (*SI Appendix*, Fig. S8 *I* and *J*).

Computational Modeling. To simulate neuronal activity in the frontal cortex during hippocampal ripples, a reduced model of the local MOs circuit was developed using the neural simulator Brian 2 (74). The model consisted of 3 leaky integrate-and-fire neurons: a SOM^+ interneuron, a PV^+ interneuron, and a principal neuron. All 3 neurons received excitatory input from the hippocampus, which was modeled as a Poisson spike train with a firing rate that increased from a baseline level f_{base} to a maximum f_{max} during 1 s in a step-like manner, representing increased hippocampal inputs during ripples. The PV^+ interneuron inhibited the principal neuron, while the SOM^+ interneuron inhibited both the PV^+ interneuron and the principal neuron. The properties of the conductance-based excitatory and inhibitory synapses, intrinsic properties of the model neurons and simulation parameters are given in *SI Appendix*, Table S1. Plasticity of excitatory synapses on SOM^+ interneurons during learning was simulated by increasing the excitatory synaptic conductance to the SOM^+ model interneuron (Fig. 6 and *SI Appendix*, Fig. S10). Neocortical principal neurons receive inputs from hundreds of SOM^+ and PV^+ interneurons (75). To reduce the complexity of the local MOs network in the model, these presynaptic SOM^+ and PV^+ populations were lumped into two model cells that were able to sustain high firing rates (>1 kHz) and that had output synapses with large conductances (up to 100 nS).

Statistical Analysis. All statistical tests were performed in GraphPad Prism (version 9). Wilcoxon signed-rank or Mann–Whitney *U* tests were used to assess the statistical significance of paired or unpaired data, as appropriate. Multiple comparisons were performed using Kruskal–Wallis tests adjusted with Dunn's correction. One-way repeated-measures ANOVA with the Dunnett post hoc test was applied in all behavioral analysis, and two-way ANOVA with factors' interactions and Bonferroni post hoc tests were used in different groups of f–I curves. In Fig. 5, mice or data points were excluded from analysis when viral injections were not bilaterally on target. Tests were considered significant if the *P*-value was < 0.05, otherwise "n.s." denotes "not statistically significant". Bar graphs and error bars show mean ± SEM.

Data, Materials, and Software Availability. Analysis and simulation code has been deposited in Github (https://github.com/neurodroid/haussmeister (76); https://github.com/neurodroid/ZH2024 (77)). Due to size reasons (several hundreds of gigabyte of data), data reported in this paper will be shared by the lead contact upon request. Further information and requests for resources and reagents should be directed to and will be fulfilled by the lead contact, Christoph Schmidt-Hieber (christoph.schmidt-hieber@uni-jena.de). Previously published data were used for this work (Part of the whole-cell patch-clamp data used in the present study were used for previous work, where we determined membrane potential dynamics in frontal neurons preceding locomotion https://doi.org/10.1016/j.celrep.2021.110035 (37)).

ACKNOWLEDGMENTS. We thank Koen Vervaeke for comments on the manuscript, Claire Lecestre for technical support, Gabriel Lepousez and Mariana Alonso for technical advice, and Hsin-Lun Kao and Alexiane Laude for help with analysis. Schematic drawings in Figs. 1, 2, and 4 were partly adapted from https://scidraw.io (39, 47, 51, 52) under a creative commons license (CC-BY 4.0). This work was supported by funding from the European Research Council (ERC StG 678790 NEWRON to C.S.-H.), the Pasteur Weizmann Council (to C.S.-H.), the Agence Nationale pour la Recherche (ANR-22-CE16-0005-01 MEMNET to C.S.-H.), and the École Doctorale Cerveau-Cognition-Comportement (ED3C, ED no. 158, contrat doctoral no. 2802/2017 to R.G.-O.).

Author affiliations: [a]Institut Pasteur, Université Paris Cité, Neural Circuits for Space and Memory, Department of Neuroscience, Paris F-75015, France; and [b]Institute for Physiology I, Jena University Hospital, Jena 07743, Germany

Author contributions: C.-L.Z. and C.S.-H. designed research; C.-L.Z., L.S., and C.S.-H. performed research; C.-L.Z., R.G.-O., and C.S.-H. contributed new reagents/analytic tools; C.-L.Z., R.G.-O., and C.S.-H. analyzed data; and C.-L.Z., R.G.-O., and C.S.-H. wrote the paper.

1. K. Diba, G. Buzsáki, Forward and reverse hippocampal place-cell sequences during ripples. *Nat. Neurosci.* **10**, 1241–1242 (2007).
2. T. J. Davidson, F. Kloosterman, M. A. Wilson, Hippocampal replay of extended experience. *Neuron* **63**, 497–507 (2009).
3. M. P. Karlsson, L. M. Frank, Awake replay of remote experiences in the hippocampus. *Nat. Neurosci.* **12**, 913–918 (2009).
4. N. K. Logothetis *et al.*, Hippocampal–cortical interaction during periods of subcortical silence. *Nature* **491**, 547–553 (2012).
5. A. K. Lee, M. A. Wilson, Memory of sequential experience in the hippocampus during slow wave sleep. *Neuron* **36**, 1183–1194 (2002).
6. P. W. Frankland, B. Bontempi, The organization of recent and remote memories. *Nat. Rev. Neurosci.* **6**, 119–130 (2005).
7. D. Marr, Simple memory: A theory for archicortex. *Philos. Trans. R. Soc. Lond. B Biol. Sci.* **262**, 23–81 (1971).
8. B. L. McNaughton, R. G. M. Morris, Hippocampal synaptic enhancement and information storage within a distributed memory system. *Trends Neurosci.* **10**, 408–415 (1987).

9. G. Buzsáki, Memory consolidation during sleep: A neurophysiological perspective. *J. Sleep Res.* **7**, 17–23 (1998).
10. G. Buzsáki, L. W. Leung, C. H. Vanderwolf, Cellular bases of hippocampal EEG in the behaving rat. *Brain Res.* **287**, 139–171 (1983).
11. G. Buzsáki, Hippocampal sharp waves: Their origin and significance. *Brain Res.* **398**, 242–252 (1986).
12. D. Sullivan *et al.*, Relationships between hippocampal sharp waves, ripples, and fast gamma oscillation: Influence of dentate and entorhinal cortical activity. *J. Neurosci.* **31**, 8605–8616 (2011).
13. J. Gan, S.-M. Weng, A. J. Pernía-Andrade, J. Csicsvari, P. Jonas, Phase-locked inhibition, but not excitation, underlies hippocampal ripple oscillations in awake mice in vivo. *Neuron* **93**, 308–314 (2017).
14. G. Buzsáki, Hippocampal sharp wave-ripple: A cognitive biomarker for episodic memory and planning. *Hippocampus* **25**, 1073–1188 (2015).
15. H. R. Joo, L. M. Frank, The hippocampal sharp wave–ripple in memory retrieval for immediate use and consolidation. *Nat. Rev. Neurosci.* **19**, 744–757 (2018).
16. A. G. Siapas, M. A. Wilson, Coordinated interactions between hippocampal ripples and cortical spindles during slow-wave sleep. *Neuron* **21**, 1123–1128 (1998).
17. G. Girardeau, K. Benchenane, S. I. Wiener, G. Buzsáki, M. B. Zugaro, Selective suppression of hippocampal ripples impairs spatial memory. *Nat. Neurosci.* **12**, 1222–1223 (2009).
18. N. Maingret, G. Girardeau, R. Todorova, M. Goutierre, M. Zugaro, Hippocampo-cortical coupling mediates memory consolidation during sleep. *Nat. Neurosci.* **19**, 959–964 (2016).
19. L. Roux, B. Hu, R. Eichler, E. Stark, G. Buzsáki, Sharp wave ripples during learning stabilize the hippocampal spatial map. *Nat. Neurosci.* **20**, 845–853 (2017).
20. M. Geva-Sagiv *et al.*, Augmenting hippocampal-prefrontal neuronal synchrony during sleep enhances memory consolidation in humans. *Nat. Neurosci.* **26**, 1100–1110 (2023).
21. F. Ferino, A. M. Thierry, J. Glowinski, Anatomical and electrophysiological evidence for a direct projection from ammon's horn to the medial prefrontal cortex in the rat. *Exp. Brain Res.* **65**, 421–426 (1987).
22. S. Ährlund-Richter *et al.*, A whole-brain atlas of monosynaptic input targeting four different cell types in the medial prefrontal cortex of the mouse. *Nat. Neurosci.* **22**, 657–668 (2019).
23. L. A. Cenquizca, L. W. Swanson, Spatial organization of direct hippocampal field CA1 axonal projections to the rest of the cerebral cortex. *Brain Res. Rev.* **56**, 1–26 (2007).
24. T. M. Jay, M. P. Witter, Distribution of hippocampal CA1 and subicular efferents in the prefrontal cortex of the rat studied by means of anterograde transport of Phaseolus vulgaris-leucoagglutinin. *J. Comp. Neurol.* **313**, 574–586 (1991).
25. E. Dégenètais, A.-M. Thierry, J. Glowinski, Y. Gioanni, Synaptic influence of hippocampus on pyramidal cells of the rat prefrontal cortex: An in vivo intracellular recording study. *Cereb. Cortex* **13**, 782–792 (2003).
26. S. P. Jadhav, G. Rothschild, D. K. Roumis, L. M. Frank, Coordinated excitation and inhibition of prefrontal ensembles during awake hippocampal sharp-wave ripple events. *Neuron* **90**, 113–127 (2016).
27. F. Xia *et al.*, Parvalbumin-positive interneurons mediate neocortical-hippocampal interactions that are necessary for memory consolidation. *Elife* **6**, e27868 (2017).
28. A. Peyrache, F. P. Battaglia, A. Destexhe, Inhibition recruitment in prefrontal cortex during sleep spindles and gating of hippocampal inputs. *Proc. Natl. Acad. Sci. U.S.A.* **108**, 17207–17212 (2011).
29. X. Liu, A. G. Carter, Ventral hippocampal inputs preferentially drive corticocortical neurons in the infralimbic Prefrontal Cortex. *J. Neurosci.* **38**, 7351–7363 (2018).
30. R. Marek *et al.*, Hippocampus-driven feed-forward inhibition of the prefrontal cortex mediates relapse of extinguished fear. *Nat. Neurosci.* **21**, 384–392 (2018).
31. Q. Sun *et al.*, A whole-brain map of long-range inputs to GABAergic interneurons in the mouse medial prefrontal cortex. *Nat. Neurosci.* **22**, 1357–1370 (2019).
32. J. C. H. Cottam, S. L. Smith, M. Häusser, Target-specific effects of somatostatin-expressing interneurons on neocortical visual processing. *J. Neurosci.* **33**, 19567–19578 (2013).
33. B. Hangya, H.-J. Pi, D. Kvitsiani, S. P. Ranade, A. Kepecs, From circuit motifs to computations: Mapping the behavioral repertoire of cortical interneurons. *Curr. Opin. Neurobiol.* **26**, 117–124 (2014).
34. C. K. Pfeffer, M. Xue, M. He, Z. J. Huang, M. Scanziani, Inhibition of inhibition in visual cortex: The logic of connections between molecularly distinct interneurons. *Nat. Neurosci.* **16**, 1068–1076 (2013).
35. B. Rudy, G. Fishell, S. Lee, J. Hjerling-Leffler, Three groups of interneurons account for nearly 100% of neocortical GABAergic neurons. *Dev. Neurobiol.* **71**, 45–61 (2011).
36. H. Hu, J. Gan, P. Jonas, Interneurons., Fast-spiking, parvalbumin^{+} GABAergic interneurons: From cellular design to microcircuit function *Science* **345**, 1255263 (2014).
37. C.-L. Zhang *et al.*, Inhibitory control of synaptic signals preceding locomotion in mouse frontal cortex. *Cell Rep.* **37**, 110035 (2021).
38. R. Gómez-Ocádiz *et al.*, A synaptic signal for novelty processing in the hippocampus. *Nat. Commun.* **13**, 4122 (2022).
39. C. Reynaud *et al.*, Tomography. Zenodo. https://doi.org/10.5281/zenodo.3712368. Deposited 15 July 2020.
40. M. Carlén, What constitutes the prefrontal cortex? *Science* **358**, 478–482 (2017).
41. F. Barthas, A. C. Kwan, Secondary motor cortex: where "sensory" meets "motor" in the rodent frontal cortex. *Trends Neurosci.* **40**, 181–193 (2017).
42. J. C. Erlich, M. Bialek, C. D. Brody, A cortical substrate for memory-guided orienting in the rat. *Neuron* **72**, 330–343 (2011).
43. J. M. Olson, J. K. Li, S. E. Montgomery, D. A. Nitz, Secondary motor cortex transforms spatial information into planned action during navigation. *Curr. Biol.* **30**, 1845–1854.e4 (2020).
44. P. Coen, T. P. H. Sit, M. J. Wells, M. Carandini, K. D. Harris, Frontal cortex learns to add evidence across modalities. bioRxiv [Preprint] (2022). https://doi.org/10.1101/2021.04.26.441250 (Accessed 13 October 2024).
45. I. Voitov, T. D. Mrsic-Flogel, Cortical feedback loops bind distributed representations of working memory. *Nature* **608**, 381–389 (2022).
46. X. Yin, Y. Wang, J. Li, Z. V. Guo, Lateralization of short-term memory in the frontal cortex. *Cell Rep.* **40**, 111190 (2022).
47. W. Tang, Hippocampus and prefrontal cortex in rat's brain. *Zenodo.* (2020). 10.5281/zenodo.3925923. Deposited 1 July 2020.
48. J. J. Letzkus, S. B. E. Wolff, A. Lüthi, Disinhibition, a circuit mechanism for associative learning and memory. *Neuron* **88**, 264–276 (2015).
49. S. B. E. Wolff *et al.*, Amygdala interneuron subtypes control fear learning through disinhibition. *Nature* **509**, 453–458 (2014).
50. L. Topolnik, S. Tamboli, The role of inhibitory circuits in hippocampal memory processing. *Nat. Rev. Neurosci.* **23**, 476–492 (2022).
51. Neuron. *Zenodo*. https://doi.org/10.5281/zenodo.3925929. Deposited 1 July 2020.
52. J. Shin, Simple Pyramidal Neuron. *Zenodo*. (2020), 10.5281/zenodo.3926001. Deposited 1 July 2020.
53. K. A. Cummings, R. L. Clem, Prefrontal somatostatin interneurons encode fear memory. *Nat. Neurosci.* **23**, 61–74 (2020).
54. H. Xu *et al.*, A disinhibitory microcircuit mediates conditioned social fear in the prefrontal cortex. *Neuron* **102**, 668–682.e5 (2019).
55. A. I. Abbas *et al.*, Somatostatin interneurons facilitate hippocampal-prefrontal synchrony and prefrontal spatial encoding. *Neuron* **100**, 926–939.e3 (2018).
56. I. Ehrlich *et al.*, Amygdala inhibitory circuits and the control of fear memory. *Neuron* **62**, 757–771 (2009).
57. S. Krabbe *et al.*, Adaptive disinhibitory gating by VIP interneurons permits associative learning. *Nat. Neurosci.* **22**, 1834–1843 (2019).
58. G. Silberberg, H. Markram, Disynaptic inhibition between neocortical pyramidal cells mediated by Martinotti cells. *Neuron* **53**, 735–746 (2007).
59. E. Fino, R. Yuste, Dense inhibitory connectivity in neocortex. *Neuron* **69**, 1188–1203 (2011).
60. E. Abs *et al.*, Learning-related plasticity in dendrite-targeting layer 1 interneurons. *Neuron* **100**, 684–699.e6 (2018).
61. H. Xu, H.-Y. Jeong, R. Tremblay, B. Rudy, Neocortical somatostatin-expressing GABAergic interneurons disinhibit the thalamorecipient layer 4. *Neuron* **77**, 155–167 (2013).
62. F. P. Battaglia, G. R. Sutherland, B. L. McNaughton, Hippocampal sharp wave bursts coincide with neocortical "up-state" transitions. *Learn. Mem.* **11**, 697–704 (2004).
63. C. M. A. Pennartz *et al.*, The ventral striatum in off-line processing: Ensemble reactivation during sleep and modulation by hippocampal ripples. *J. Neurosci.* **24**, 6446–6456 (2004).
64. A. R. Chambers, C. N. Berge, K. Vervaeke, Cell-type-specific silence in thalamocortical circuits precedes hippocampal sharp-wave ripples. *Cell Rep.* **40**, 111132 (2022).
65. C. King, D. A. Henze, X. Leinekugel, G. Buzsáki, Hebbian modification of a hippocampal population pattern in the rat. *J. Physiol.* **521**, 159–167 (1999).
66. J. H. L. P. Sadowski, M. W. Jones, J. R. Mellor, Sharp-wave ripples orchestrate the induction of synaptic plasticity during reactivation of place cell firing patterns in the hippocampus. *Cell Rep.* **14**, 1916–1929 (2016).
67. Y. Nishimura, Y. Ikegaya, T. Sasaki, Prefrontal synaptic activation during hippocampal memory reactivation. *Cell Rep.* **34**, 108885 (2021).
68. E. Kim, B. A. Bari, J. Y. Cohen, Subthreshold basis for reward-predictive persistent activity in mouse prefrontal cortex. *Cell Rep.* **35**, 109082 (2021).
69. C. Schmidt-Hieber, M. Häusser, Cellular mechanisms of spatial navigation in the medial entorhinal cortex. *Nat. Neurosci.* **16**, 325–331 (2013).
70. M. Allegra, L. Posani, R. Gómez-Ocádiz, C. Schmidt-Hieber, Differential relation between neuronal and behavioral discrimination during hippocampal memory encoding. *Neuron* **108**, 1103–1112.e6 (2020).
71. T. W. Margrie, M. Brecht, B. Sakmann, In vivo, low-resistance, whole-cell recordings from neurons in the anaesthetized and awake mammalian brain. *Pflugers Arch.* **444**, 491–498 (2002).
72. M.-S. To, S. Honnuraiah, G. J. Stuart, Voltage clamp errors during estimation of concurrent excitatory and inhibitory synaptic input to neurons with dendrites. *Neuroscience* **489**, 98–110 (2022).
73. S. R. Williams, S. J. Mitchell, Direct measurement of somatic voltage clamp errors in central neurons. *Nat. Neurosci.* **11**, 790–798 (2008).
74. M. Stimberg, R. Brette, D. F. Goodman, Brian 2, an intuitive and efficient neural simulator. *Elife* **8**, e47314 (2019).
75. L. Campagnola *et al.*, Local connectivity and synaptic dynamics in mouse and human neocortex. *Science* **375**, eabj5861 (2022).
76. C. Schmidt-Hieber, Github analysis code. Zenodo. https://doi.org/10.5281/zenodo.13940195. Deposited 16 October 2024.
77. C. Schmidt-Hieber, Github simulation code. Zenodo. https://doi.org/10.5281/zenodo.13940218. Deposited 16 October 2024.